Electron-impact total cross sections for phosphorous triflouride

Minaxi Vinodkumar[*]
V P & R P T P Science College, Vallabh Vidyanagar-388 120, India

Chetan Limbachiya[†]
Department of Applied Physics, The M. S. University Baroda, Vadodara-390001, India

Hardik Desai[‡] and P. C. Vinodkumar[§]
Department of Physics, Sardar Patel University, Vallabh Vidyanagar-388120, India
(Received 28 March 2014; revised manuscript received 14 May 2014; published 23 June 2014)

Various total cross sections for scattering of electrons by phosphorous triflouride (PF_3) using the R-matrix method for incident energies from 0.1–15 eV and using spherical complex optical potential formalism beyond ionization threshold of target to 5000 eV are reported. We performed close-coupling calculations using static exchange plus polarization model. We employed different target models in order to study their relative dependence on the total cross sections. Three important structures are revealed in the total-cross-section curve: one that corresponds to the Ramsauer-Townsend minimum at 0.33 eV, the second is a strong maximum of 100 Å^2 at 1 eV, the third is around 11 eV corresponding to negative ion formation as predicted by earlier study. The total ionization cross sections are computed using the complex scattering potential ionization contribution method and the binary encounter Bethe method. The electronic-excitation cross sections, momentum-transfer cross sections, and differential and ionization cross sections are our maiden efforts for this system. We have compared our total-cross-section results with available theoretical and experimental results.

DOI: 10.1103/PhysRevA.89.062715 PACS number(s): 34.80.Bm

I. INTRODUCTION

Considerable progress has been made in the study of electron-molecule collision studies in the past decades both experimentally and theoretically. By utilizing better electron spectrometers and adopting position-sensitive detectors, experimentalists are capable of producing accurate cross-sectional data on electron collisions with larger molecules and even explore free radical species. However, given the vast number of molecular systems and the requirement for an ever-increasing amount of data, the experimental community is unable to meet the demands of the myriad of data users. In this respect, one must look to theory to provide much of the required electron-scattering data. On the theoretical front, with the advent of high-performing computers and the development of very accurate theories, computation of reliable cross-section data is now possible at least for smaller targets. These theoretical methods are computationally taxing and consume longer computing time. Thus, there is a demand for more generic and faster calculations to provide reliable data to the user community.

Electron-molecule collision cross sections from very low energy up to threshold play a pivotal role in determining electron transport properties and electron energy distribution of a swarm of electrons drifting through various gases. They also play a significant role in modeling low-temperature plasmas. In addition to the practical interest, electron scattering data are of fundamental theoretical importance towards the understanding of various electron-assisted molecular interactions [1]. The electron bombardment on a molecule may result into the formation of positive and negative ions. The latter may be produced by resonance attachment, dissociative resonance capture, and ion-pair formation. These mechanisms operate at different electron energies. The resonance processes usually occur in the 0–10 eV energy region and the ion-pair processes at energies above 10 eV.

Perfluorinated compounds are widely used in electrical industries, plasma-assisted fabrication of microcircuits, surface hardening, agriculture, and medicinal fields. For example, in microelectronics doping of phosphorous is done either with pure phosphorous or with its halides or hydrides. However, the pure phosphorous is highly inflammable and the hydrides, i.e., PH_3, are highly toxic compared to halides [2]. PF_3 is thus suggested to be a potential reagent for the gas-phase synthesis in microelectronic dopings.

There exist numerous studies on PF_3 which include positive and negative ion formation on electron bombardment, determination of ionization potential of PF_3 using photoelectron spectroscopy, determination of the structure of PF_3, and electron-stimulated desorption of positive ion of PF_3^+, etc. Macneil and Thynne [3] and Harland *et al.* [4] studied negative ion formation of PF_3 as a function of electron energy using a Bendix time-of-flight mass spectrometer. Torgerson and Westmore [5] determined relative intensities and appearance potentials of several positive ions in the mass spectrum of PF_3^+. There are extensive studies on determination of ionization potential of PF_3 using photoelectron spectroscopy. While Bassett *et al.* [6,7] measured adiabatic ionization potential at 11.66 eV, the vertical ionization potential of 12.28 eV is reported by Potis *et al.* [8] and at 12.3 eV are reported by two groups (Green *et al.* [9] and Maier *et al.* [10]) and at 12.27 eV is reported by Zhao and Setser [11]. Aside from this,

[*]minaxivinod@yahoo.co.in
[†]chetanlimbachiya2@yahoo.com
[‡]hardikdesai.phy@gmail.com
[§]p.c.vinodkumar@gmail.com

the photoionization studies on PF_3 are reported by Price and Pasmore [12] and molecular orbital calculations are performed for PH_3, PF_3, and $P(CH_3)_3$ by Hillier and Saunders [13] and for PF_3 and PF_2CN by Hall and Hameka [14]. An extensive study on electron-stimulated desorption (ESD) of positive ions from PF_3 molecules adsorbed on a Pt substrate over a wide electron energy range (0–175 eV) is performed by Akbulut *et al.* [15]. These studies are important to get information on the bonding mechanisms of adsorbed PF_3 as well as the coverage-dependent azimuthal orientations of adsorbed PF_3 [15].

In view of these extensive studies as seen from the literature survey, it is evident that not much of experimental or theoretical work is reported on e-PF_3 scattering cross sections. On the experimental front, a single set of scattering cross-sectional data is reported by Szmytkowski *et al.* [16]. They measured total cross sections using linear transmission method for energy range 0.6 to 370 eV. The theoretical total cross sections based on the modified additivity rule are reported by Shi *et al.* [17] for impact energies from 30 to 5000 eV. Apart from the electron impact total cross sections, there are no studies reported for the electronic excitations, differential cross sections, momentum-transfer cross sections, as well as ionization cross sections in literature. Hence, present study on e-PF_3 over energies 0.1 to 5000 eV is important to fill the void of various total-cross-section data, viz., electronic-excitation, differential, momentum-transfer, and ionization cross sections.

II. THEORETICAL METHODOLOGY

For the low energy (0.1 eV to about 15 eV), we employed the *ab initio* calculations using Quantemol-N [18] which utilizes UK molecular R-matrix code [19]. The spherical complex optical potential (SCOP) method is employed for calculating total (elastic plus inelastic) cross sections beyond ionization threshold up to 5 keV [20]. An outline of these two formalisms is briefly discussed in the following subsections. Before going to the details of theoretical methods, we also discuss the target model employed for the present system.

A. Target model

The accuracy of the scattering data depends on the accuracy of the target wave function, hence, it is imperative to have an appropriate target model. For many-electron targets such as PF_3, the relative energy between the N-target electrons and the $N+1$-target plus scattering electron becomes important since neither the target nor the scattering wave functions have the energies close to the exact value for the given system. This requires careful choice of the configurations in terms of a complete active space (CAS) and the valance configuration interaction (CI) representation of the target system [18]. It is realized by characterizing the low-lying electronic states of the target and by generating a suitable set of orbitals. The molecular orbitals are generated by performing a self-consistent field (SCF) calculation of the ground state of the molecule ($X\ 1A_1$). Since the SCF procedure is inadequate to provide a good representation of the target states, we improve the energies of these states by invoking the variational method of configuration interaction (CI) in which we take linear combination of configuration state functions (CSFs) of a particular overall symmetry. This lowers the energies and the correlation introduced provides a better description of the charge cloud and the energies. For all the states included here, we employ CI wave function to represent the target states.

The Hartree-Fock electronic configuration for the ground state of PF_3 at its equilibrium geometry in Cs symmetry is $1a'^2$, $2a'^2$, $1a''^2$, $3a'^2$, $4a'^2$, $5a'^2$, $2a''^2$, $6a'^2$, $7a'^2$, $8a'^2$, $3a''^2$, $9a'^2$, $10a'^2$, $11a'^2$, $4a''^2$, $12a'^2$, $5a''^2$, $13a'^2$, $6a''^2$, $7a''^2$, $14a'^2$. Out of 42 electrons, 38 electrons are frozen in $1a'$, $2a'$, $3a'$, $4a'$, $5a'$, $6a'$, $7a'$, $8a'$, $9a'$, $10a'$, $11a'$, $12a'$, $13a'$, $1a''$, $2a''$, $3a''$, $4a''$, $5a''$, $6a''$ orbitals and 4 electrons are kept free to move in active space of $14a'$, $15a'$, $16a'$, $7a''$, $8a''$, $9a''$ molecular orbitals. All calculations of PF_3 are performed in Cs symmetry since the R-matrix code can only handle calculations in a subgroup of the highest accessible Abelian point group $D2h$. We have used 6-311G Gaussian-type orbital (GTO) basis set and double zeta plus polarization (DZP) basis set in order to study the dependency of target properties and scattering cross sections on the basis set chosen.

The target wave functions are computed using the complete active space configuration integration (CAS-CI) method. They are subsequently improved using a pseudonatural orbital calculation. The Born correction for this polar molecule is employed to account for higher partial waves, $l > 4$. In the static-exchange-polarization (SEP) model, the ground state of the molecule is perturbed by single and double excitations of the electrons, thus leading to the inclusion of polarization effects. The SEP model augments the static-exchange (SE) model by including polarization effects. Thus, polarization effects are accounted by including closed channels in a CI expansion of the wave function of the entire scattering system. These electronic and angular momentum channels altogether generated 393 configuration state functions (CSFs) and 90 channels in the calculation. The four lowest Cs electronic excited states $1A'$, $3A''$, $3A'$, $1A''$ are employed and all possible single and double excitations to virtual orbitals are included.

The Quantemol-N modules GAUSPROP and DENPROP [21] construct the transition density matrix from the target eigenvectors obtained from configuration integration (CI) expansion and generate the target properties. The multipole transition moments obtained are then used to solve the outer region coupled equations and the dipole polarizability α_0. These are computed using second-order perturbation theory and the property integrals are evaluated by GAUSPROP [21]. Our self-consistent field (SCF) model calculations yielded target parameters such as the ground-state energy, the first electronic-excitation energy, rotational constant, and dipole moment which are listed in Table I.

The self-consistent field calculations yielded the ground-state energy of -639.0582 hartree using 6-311G and -639.227 hartree using DZP basis set, which is probably not reported earlier in the literature. We report four electronic excitation states below ionization threshold of the target for phosphorous triflouride with the first electronic-excitation energy obtained at 6.965 eV using DZP and at 6.971 eV using 6-311G basis set as listed in Table II. There are no data, either theoretical or experimental, for the first electronic-excitation energy available for comparison to the best of our knowledge. The present rotational constant of 0.2792 cm^{-1} is in good

TABLE I. Target properties obtained for the PF_3 molecule using 6-311G and DZP basis sets

	Present		Other
Target property (unit)	6-311G	DZP	Theor. and Expt.
Ground-state energy energy (hartree)	− 639.058	− 639.227	
First excitation energy (eV)	6.965	6.971	
Rotational constant (cm^{-1})	0.2792	0.2792	0.2608 [22]
Dipole moment (debye)	3.44	2.24	1.03 [23] 1.32 [24]

agreement with the theoretical value of 0.2608 cm^{-1} reported in CCCBDB [22]. The dipole moment is 3.44 D obtained using 6-31G and 2.24 D obtained using DZP are quite high compared to experimental value of 1.03 D reported in CRC [23] and 1.32 D calculated earlier by Bendiab *et al.* [24]. It can be easily seen that the dipole moment is very sensitive to the basis set chosen. Also, inclusion of large diffused functions can improve upon the dipole moment but we can not use diffuse functions for the target representation as this would violate the boundary condition that the molecular orbitals should vanish on the surface of the R-matrix sphere [25].

B. Low-energy formalism (0.01 ∼ 15 eV)

The most popular methodologies employed for low-energy electron collision calculations are the Kohn variational method [26,27], the Schwinger multichannel method [28,29], and the R-matrix method [19], of which the R matrix is the most widely used. The R-matrix method [19] splits configuration space into an inner region, which is a sphere of radius "a" about the target center of mass, and an outer region. The boundary between these two regions is defined by R-matrix radius. This radius is chosen large enough so that, in the external region, only known long-range forces are effective and antisymmetrization effects can be neglected. In the inner region, the full electron-molecule problem is solved using quantum chemistry codes. The inner region is usually chosen to have a radius of around 10 a.u. and the outer region is extended to about 100 a.u. The choice of this value depends on the stability of results obtained in the inner and outer region calculations. We describe the scattering within the fixed-nuclei (FN) approximation that neglects any dynamics involving the nuclear motion (rotational as well as vibrational), whereas the bound electrons are taken to be in the ground electronic state of the target at its optimized nuclear geometry. This is an effect of the extent of electronic charge density distribution around the center of mass of the target. In this study, we have considered three different choices (10, 12, 13 a.u.) of inner R-matrix radii to find its dependence on the cross sections.

TABLE II. Vertical excitation energies for PF_3 below ionization threshold for 6-311G and DZP basis sets.

	Energy (eV)	
State	6-311G	DZP
$1A'$	0.0000	0.000
$3A''$	6.9658	6.971
$3A'$	8.182	7.295
$1A''$	9.8963	10.032
$1A'$		10.323

In the inner region, the total wave function for the system is written as

$$\Psi_k^{N+1} = A \sum_I \Psi_I^N(x_1, \ldots, x_N) \sum_j \zeta_j(x_{N+1}) a_{Ijk} + \sum_m \chi_m(x_1, \ldots, x_{N+1}) b_{mk}, \quad (1)$$

where A is the antisymmetrization operator, x_N is the spatial and spin coordinate of the nth electron, ζ_j is a continuum orbital spin coupled with the scattering electron, and a_{Ijk} and b_{mk} are variational coefficients determined in the calculation. The summations in the first term run over the target states used in the close-coupled expansion. The summation in the second term runs over configurations χ_m, where all electrons are placed in target molecular orbitals. The number of these configurations varies considerably with the model employed. With the wave function given by Eq. (1), a static-exchange calculation has a single Hartree-Fock target state in the first sum. The second term runs over the minimal number of configurations (usually three or fewer)required to relax orthogonality constraints between the target molecular orbitals and the functions used to represent the configuration. Our fully close-coupled system uses the lowest number of target states represented by a CI expansion in the first term and over 100 configurations in the second. These configurations allow for both orthogonality relaxation and short-range polarization effects.

The target and the continuum orbitals are represented by Gaussian-type orbitals (GTOs) and the molecular integrals are generated by the appropriate molecular package. The R matrix will provide the link between the inner and outer regions. For this purpose, the inner region is propagated to the outer region potential until its solutions match with the asymptotic functions given by the Gailitis expansion [19]. Thus, by generating the wave functions, using Eq. (1), their eigenvalues are determined. These coupled single center equations describing the scattering in the outer region are integrated to identify the K-matrix elements. The K matrix is a symmetric matrix whose dimensions are the number of channels. All the observables are basically deduced from it and further it is used to deduce the T matrix using the relation

$$T = \frac{2iK}{1 - iK}. \quad (2)$$

The T matrices are in turn used to obtain various total cross sections. The K matrix is diagonalized to obtain the eigenphase sum. The eigenphase sum is further used to obtain the position and width of the resonance by fitting them to the Breit-Wigner profile [30] using the program RESON [30].

Differential and momentum-transfer cross sections (MTCS) are calculated using the POLYDCS program [31]. The differential cross section (DCS) study is very important as it provides large information about the interaction processes. Indeed, the evaluation of DCS is a stringent test for any scattering theory as it is sensitive to effects which are averaged

out in integral cross sections. The DCS for polyatomic molecule is represented by

$$\frac{d\sigma}{d\Omega} = \sum_L A_L P_L(\cos\theta), \tag{3}$$

where P_L represents the Legendre polynomial of order L. The details about A_L are already discussed by Gianturco and Jain [32]. For a polar molecule, this expansion over L converges slowly due to the long-range nature of the dipole potential. To overcome this problem, we use the closure formula given by

$$\frac{d\sigma}{d\Omega} = \frac{d\sigma^B}{d\Omega} + \sum_L \left(A_L - A_L^B\right) P_L \cos\theta. \tag{4}$$

Here, the superscript B denotes the fact that the relevant term is calculated under the Born approximation with an electron point dipole interaction. It is clear from the expression (4) that convergence of the series is faster as the contribution arising from the Born term is subtracted as seen in Eq. (4). The quantity $\frac{d\sigma^B}{d\Omega}$ for any initial rotor state is given by the sum over all final rotor states as

$$\frac{d\sigma^B}{d\Omega} = \sum_{J'\tau'} \frac{d\sigma^B}{d\Omega}(J\tau \rightarrow J'\tau'). \tag{5}$$

The calculated dipole moment (3.44 D) and rotational constants ($A = 0.2792$ cm^{-1}, $B = 0.2577$ cm^{-1}, $C = 0.1768$ cm^{-1}) for PF_3 are used in the calculation of elastic DCS ($J = 0 \rightarrow J' = 0$) and rotationally inelastic ($J = 0 \rightarrow J' = 1, 2, 3, 4$ and 5) DCSs at different collision energies.

In fact, the MTCS is obtained by integrating the differential cross sections (DCS) with a weight factor (1-cosθ)

$$\sigma_m = 2\pi \int \frac{d\sigma}{d\Omega}(1 - \cos\theta) d\theta. \tag{6}$$

C. Higher-energy formalism (threshold to 5 keV)

The scattering calculations above the threshold energy are studied using the SCOP formalism [20,33]. In this formalism, the electron-molecule system is represented by a complex potential comprising of real and imaginary parts as

$$V_{\text{opt}}(r, E_i) = V_R(r) + i V_I(r, E_i) \tag{7}$$

such that

$$V_R(r, E_i) = V_{st}(r) + V_{\text{ex}}(r, E_i) + V_p(r, E_i), \tag{8}$$

where E_i is the incident energy. Equation (8) corresponds to various real potentials to account for the electron target interaction, namely, static, exchange, and the polarization potentials, respectively. These potentials are obtained using the target geometry, molecular charge density of the target, the ionization potential, and polarizability as inputs. The molecular charge density may be derived from the atomic charge density by expanding it from the center of mass of the system. The molecular charge density so obtained is normalized to account for the total number of electrons present. The atomic charge densities and static potentials (V_{st}) are formulated from the parametrized Hartree-Fock wave functions given by Cox and Bonham [34].

The parameter-free Hara's free-electron-gas exchange model [35] is used for the exchange potential (V_{ex}). The polarization potential (V_p) is formulated from the parameter-free model of correlation-polarization potential given by Zhang *et al.* [36]. Here, various multipole nonadiabatic corrections are incorporated in the intermediate region which will approach the correct asymptotic form at large r smoothly. The target parameters such as ionization potential (IP) and dipole polarizability (α_0) of the target used here are the best available from the literature [37].

The imaginary part in V_{opt}, called the absorption potential V_{abs}, accounts for the total loss of flux scattered into the allowed electronic excitation or ionization channels. The expressions used here are vibrationally and rotationally elastic. This is due to the fact that the nonspherical terms do not contribute much to the total potential at the present high-energy range.

The well-known quasifree model of Staszeweska *et al.* [38] is employed for the absorption part, given by

$$V_{\text{abs}}(r, E_i) = -\rho(r)\sqrt{\frac{T_{\text{loc}}}{2}}\left(\frac{8\pi}{10k_F^3 E_i}\right) \theta\left(p^2 - k_F^2 - 2\Delta\right)(A_1 + A_2 + A_3), \tag{9}$$

where T_{loc} is the local kinetic energy of the incident electron which is given by

$$T_{\text{loc}} = E_i - (V_{st} + V_{\text{ex}} + V_p). \tag{10}$$

Here, $p^2 = 2E_i$ and $k_F = [3\pi^2\rho(r)]^{\frac{1}{3}}$ is the Fermi wave vector and A_1, A_2, and A_3 are dynamic functions that depend differently on $\theta(x)$, I, Δ, and E_i. Here, I is the ionization threshold of the target, $\theta(x)$ is the Heaviside unit step function, and Δ is an energy parameter below which $V_{\text{abs}} = 0$. Hence, Δ is the principal factor which decides the values of total inelastic cross section since below this value, ionization or excitation is not allowed. This is one of the main characteristics of the Staszewska model [38]. This has been modified by us by considering Δ as a slowly varying function of E_i around I. Such an approximation is meaningful since Δ fixed at I would not allow excitation at energies $E_i \leq I$. However, if Δ is much less than the ionization threshold, then V_{abs} becomes unexpectedly high near the peak position. The amendment introduced is to give a reasonable minimum value $0.8I$ to Δ [39] and also to express the parameter as a function of E_i around I, i.e.,

$$\Delta(E_i) = 0.8I + \beta(E_i - I). \tag{11}$$

Here, the parameter β is obtained by requiring that $\Delta = I$ (eV) at $E_i = E_p$, the value of incident energy at which present Q_{inel} reaches its peak. E_p can be found by calculating Q_{inel} by keeping $\Delta = I$. Beyond E_p, Δ is kept constant and is equal to I. The expression given in Eq. (11) is meaningful as Δ fixed at the ionization potential would not allow any inelastic channel to open below I. Also, if it is much less than I, then V_{abs} becomes significantly high close to the peak position of Q_{inel}.

The complex potential thus formulated is used to solve the Schrödinger equation numerically through partial-wave analysis. This calculation will produce complex phase shifts for each partial wave which carries the signature of interaction

of the incoming projectile with the target. At low energies, only a few partial waves (5–6 for absorption and 100 for polarization at ionization threshold) are significant, but as the incident energy increases more partial waves (around 40 for absorption and 100 for polarization) are needed for convergence. The phase shifts δ_l thus obtained are employed to find the relevant cross sections, total elastic (Q_{el}) and the total inelastic cross sections ($Q_{\rm inel}$), using the scattering matrix $S_l(k) = \exp(2i\delta_l)$ [40]. Then, the total scattering cross section (TCS) Q_T is obtained by adding these two cross sections [40].

III. RESULTS AND DISCUSSION

This work reports total cross sections for e-PF_3 scattering. We have employed the *ab initio* R matrix code below the ionization threshold of the target. The total cross section is the sum of total elastic and total electronic-excitation cross sections below the ionization threshold of the target. Above it, we have computed the total cross section as the sum of total elastic and total inelastic cross section using the SCOP formalism. Using these two formalisms, we are able to predict the total cross sections over a wide energy range [33,41–43]. The numerical results of total cross sections for PF_3 are reported from 0.1 to 5000 eV and are listed in Table III and are also plotted graphically.

It is important to study eigenphase diagrams as they provide the positions of resonances which are important features of collision study in the low-energy regime. Resonances are a common characteristic of electron molecule scattering at low impact energies and lead to distinctive structure in pure vibrational excitation cross sections [44]. A recursive procedure for detecting and performing Breit-Wigner fits to the eigenphase diagram is done through program RESON [30]. This program generates new energy points and marks those points where the numerically computed values of second derivative changes sign from positive to negative. Finer grids are constructed about each of these points which are used as inputs for Briet-Wigner fit [30] and the two most important parameters (position and width) related to resonances are obtained.

TABLE III. Total cross section (TCS) for the e-PF_3 scattering (energies are in eV and TCS′ are in Å^2).

Energy	TCS	Energy	TCS	Energy	TCS	Energy	TCS
0.1	93.02	5.5	33.94	12	29.20	300	9.89
0.2	64.25	6	32.19	13	29.17	400	8.45
0.4	57.42	6.5	30.83	14	29.00	500	7.43
0.6	71.03	7	29.72	15	28.73	600	6.66
0.8	93.05	7.5	28.99	16	28.38	700	6.05
1	103.50	7.52	28.96	17	27.97	800	5.56
1.2	101.54	7.54	28.93	18	27.54	900	5.15
1.5	90.70	7.56	28.90	19	27.09	1000	4.80
2	72.62	7.58	28.87	20	26.90	2000	2.94
2.5	60.10	7.6	28.84	30	23.50	3000	2.31
3	51.86	7.62	26.50	40	21.39	4000	1.78
3.5	46.20	8	27.43	60	18.93	5000	1.41
4	42.03	9	28.23	80	17.41		
4.5	38.77	10	28.77	100	16.18		
5	36.11	11	29.08	200	12.15		

TABLE IV. Position and width of resonance states for PF_3.

Resonance state	Position (eV)	Width (eV)
$2A''$	0.776	0.902
$2A'$	13.574	1.157

Table IV gives the positions and widths of resonances obtained in the present case using R-matrix calculations.

Doublet A'' state shows a shape resonance structure at 0.77 eV with a resonance width of 0.902 eV. This resonance is reflected as a strong peak in the TCS curve around 1 eV with a maximum cross-section value of 100 Å^2. Second shape resonance is predicted at 13.57 eV with a width of 1.15 eV. This peak corresponds to the negative ion formation predicted by MacNeil and Thyne [3] at 14 eV. It is indeed remarkable that our SEP calculation is able to report the Ramsauer-Townsend (RT) minimum at approximately 0.33 eV which is not reported earlier in the literature for this target.

Figure 1 presents electron-impact excitation cross sections from the ground state ($X\ 1A'$) to the first three excited states ($3A''$, $3A'$, $1A''$) obtained using the R-matrix calculation. The first electronic-excitation energy is 6.965 eV which is obtained from the transition of ground state of $X\ 1A'$ to $3A''$. The excitation cross section for this transition rises sharply with maximum value of 1.6 Å^2 and then falls fast up to 10 eV and then decreases slowly and shows a structure at 14.8 eV. The second transition is from ground state $X\ 1A'$ to $3A'$ which starts at nearly 8.2 eV and rises to maxima of 1.1 Å^2 and then decreases slowly and finally shows a hump at 14.8 eV. This transition corresponds to formation of PF^- ion which is predicted at 8.9 eV earlier by MacNeil and Thynne [3] which is closer to present value of 8.2 eV. It shows a sharp peak around

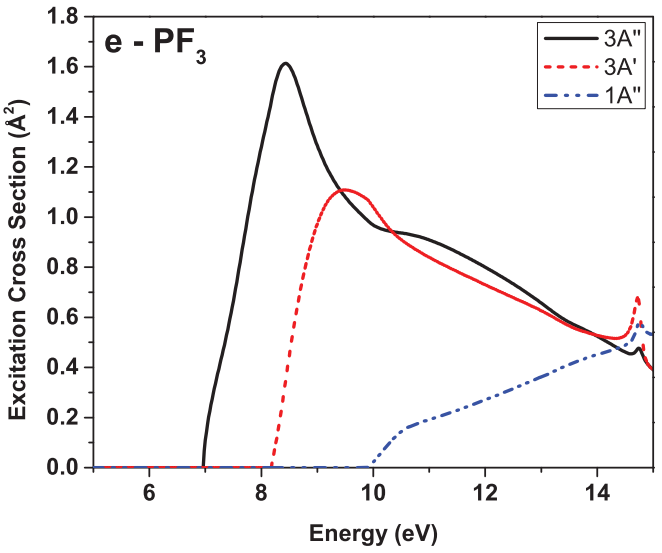

FIG. 1. (Color online) e-PF_3 excitation cross sections from the ground state ($X\ 1A'$) to the first three excited states ($3A''$, $3A'$, $1A''$): $3A''$, solid line; $3A'$, short dashed line; $1A''$, dashed dotted dotted line.

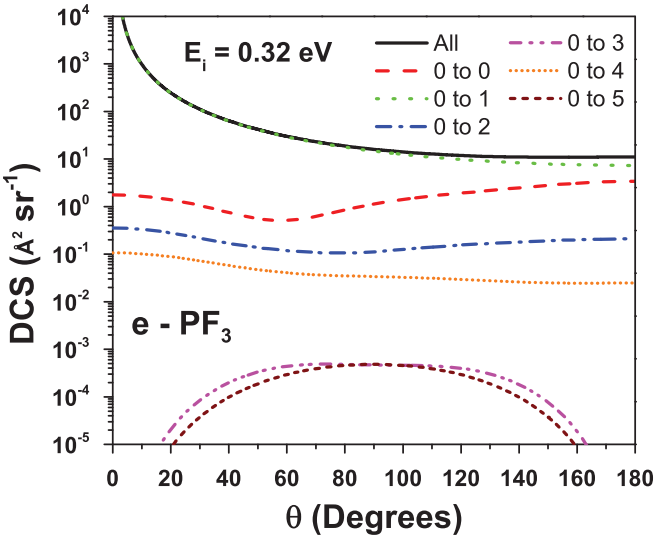

FIG. 2. (Color online) Rotationally resolved differential cross sections (DCS) for incident energy of 0.32 eV.

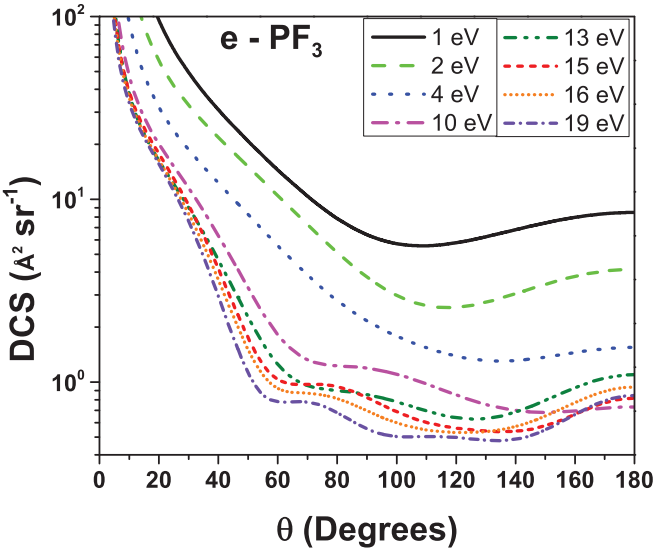

FIG. 3. (Color online) Rotationally resolved differential cross sections (DCS) for incident energies 1, 2 4, 10, 13, 15, 16, and 19 eV.: 1 eV, solid line; 2 eV, dashed line; 4 eV, dotted line; 10 eV, dashed dotted line; 13 eV, dashed dotted dotted line; 15 eV, short dashed line; 16 eV, short dotted liune; 19 eV, short dashed dotted line.

14.8 eV which may be the signature of another negative ion formation. The third transition is not much prominent which is from ground state $X\ 1A'$ to $1A''$ which starts at 9.9 eV and rises to a maxima of 0.6 Å^2 at around 14.8 eV. This transition corresponds to formation of the PF_2^- ion which was earlier predicted at 10.3 eV [3]. All the three electronic transitions show some peak structure around 15 eV which may correspond to dipolar desorption process giving rise to formation of F^- as predicted by Akbulut *et al.* [15]. The electronic excitations to $3A''$, $3A'$, $1A''$ show a sharp increase near their respective thresholds which show the dominance of these energy levels in the present calculation. These cross sections show the probability of excitation to various energy levels of the target.

Figure 2 shows our rotationally resolved DCS at 0.32 eV for all transitions ($J = 0$ to $J' = 0$ to 5) and also the summed total of all transitions. As evident from the curve, the total DCS at 0.32 eV is dominated by the dipole component ($J = 0 \rightarrow J' = 1$). As PF_3 is a polar molecule, the dipole component ($J = 0 \rightarrow J' = 1$) is much larger than the elastic component ($J = 0 \rightarrow J' = 0$). The calculated DCS is converged when J' increases up to 5. Moreover, in the elastic component, there is a minimum at about 60°.

Figure 3 shows the sum of our rotationally resolved differential cross sections summed over all transitions ($J = 0$ to $J' = 0$ to 5) for incident energies 1, 2, 4, 10, 13, 15, 16, and 19 eV. In the absence of any comparisons, we have plotted all DCS curves at different energies in the same figure. The scattering is dominated by elastic component $0 \rightarrow 0$ and dipole component $0 \rightarrow 1$. The elastic component shows a strong dip at 108° in the 1-eV curve, which indicates the dominance of a p wave in the interference pattern arising due to various partial-wave amplitudes. As the energy increases, the convergence with respect to J is rapid. The divergence at the forward angle is confirmed as being due to dipole-allowed transitions $0 \rightarrow 1$ dominating the scattering. The differential cross sections decrease as the incident energy increases. The sharp enhancement in the forward direction is a result of the strong long-range dipole component of the interaction potential. There are no theoretical or experimental comparisons available to the best of our knowledge.

The momentum-transfer cross sections (MTCS) indicate the importance of the backward scattering and are an important quantity that forms the input to solve the Boltzmann equation for the calculation of electron distribution function of a swarm of electrons drifting through a molecular gas. In contrast to the divergent behavior of DCS in the forward direction, the MTCS does not diverge due to the multiplicative factor $(1 - \cos\theta)$. A further test of the quality of our DCS is shown by the momentum-transfer cross section (MTCS) in Fig. 4 from

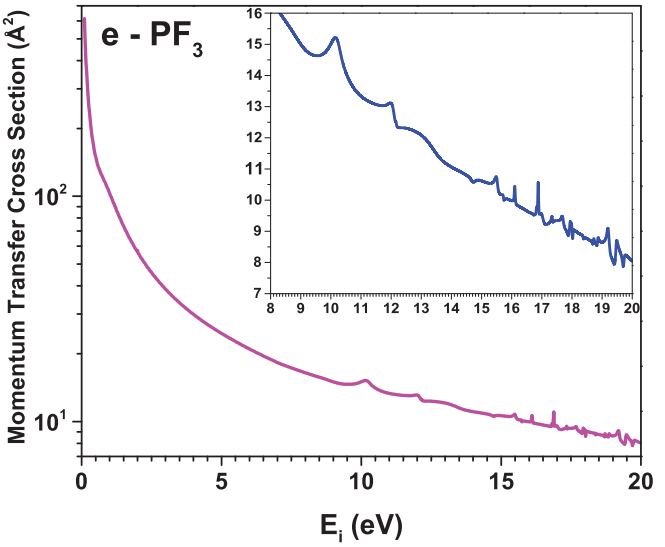

FIG. 4. (Color online) e-PF_3 momentum-transfer cross section (MTCS). Inset: Magnified view of MTCS between 8 and 20 eV.

energies 0.1 to 20 eV. In order to make more visibility of structures in the MTCS curve we have presented an inset in Fig. 4 with expanded scale with energy range 8 to 20 eV. The various peaks or structures observed in MTCS correspond to various resonance processes. For instance, at 10.5 eV there is a peak which corresponds to formation of PF_2^- [3] at 12 eV the small peak corresponds to formation of PF_3^+ ion [8] and many peaks for $E_i > 15$ eV correspond to dipolar desorption process which leads to formation of F^- ion [15]. At low impact energy the curve is divergent due to the presence of dipole moment. There are no comparisons for momentum-transfer cross section for e-PF_3 scattering to the best of our knowledge.

Due to the presence of long-range dipole interaction, the total cross section at low energy is diverging in the fixed nuclei approximation due to singularity in the differential cross section in the forward direction. It is well known that the cross sections of dipole-dominated processes only converge slowly with partial waves. To obtain converged cross sections, the effect of rotation must be included along with a large number of partial waves. The higher partial waves ($l \geqslant 4$) are included using a Born correction as given in the work of Chu and Dalgarno [45]. This is done by adjusting the T matrices using the CC cross sections generated by the code POLYDCS [31]. In this procedure, our low-l T matrices are added to analytic dipole Born T matrices using the adiabatic nuclear rotation (ANR) [33,46–48]. The Born contribution for partial waves higher than $l = 4$ to the elastic cross section at energies below 0.5 eV is quite large as seen from Fig. 5.

In Fig. 5, we have compared total-cross-section data for e-PF_3 scattering using 6-311G and DZP basis sets with available comparisons. The present calculations for total cross section at low energy are carried out using various target models. The total cross-section calculation depends on R-matrix radius (r), number of states per symmetry (n), and complete active space (c) considered in the present calculations. We have considered R-matrix radii to be 10, 12, and 13 a.u. and observed the consistency of results. The increase of the R-matrix radius increases the cross-section value which is evident from Fig. 5 [model 1 ($M1$), model 2 ($M2$), model 3 ($M3$), and model 4 ($M4$)]. Increasing the CAS value, the computation becomes more complex and it will make the resonant structures more refined but do not change the results (see results of $M3$ and $M4$). Finally, increasing the number of states per symmetry will increase the computation time and will shift the peak value of cross sections towards the left as can be seen from $M1$ and $M2$.

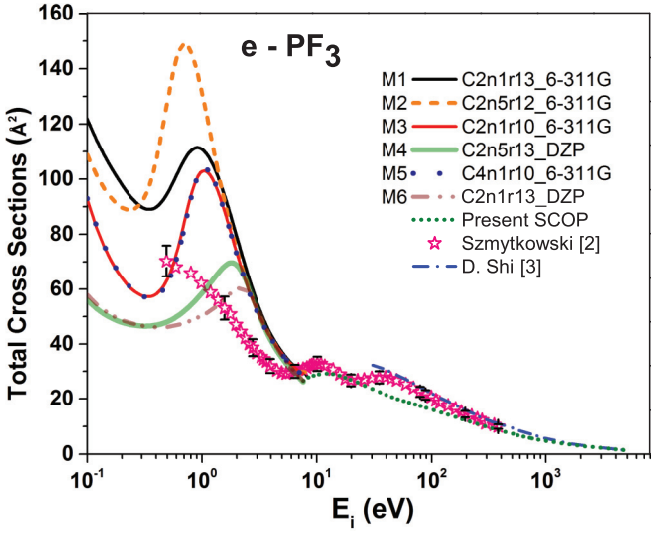

FIG. 5. (Color online) e-PF_3 total scattering cross sections: Comprehensive study ($M1$ to $M6$ and present SCOP) and their comparisons with the available experimental data: Szmytkowski *et al.* [16] (open star); theoretical data: Shi *et al.* [17] (dashed dotted line).

Three prominent structures are observed in the total-cross-section curve presented for e-PF_3 scattering in Fig. 5. The first structure is the Ramsauer-Townsend minimum which is observed at 0.33 eV. There are no theoretical or experimental data available at this energy to compare with. The Ramsauer-Townsend minimum is observed whenever the eigenphase diagram or phase shift crosses zero. In the present case, the eigenphase for doublet $A1$ state crosses the zero line which is a clear signature of the RT minimum. The physical significance of the R-T minimum is that at this energy, the attractive part of the polarization potential is canceled by the repulsive part of the exchange potential and it is a purely an S wave, low-energy phenomenon.

The second is a strong maximum at 1 eV of 100 $Å^2$. The third structure is a broad maxima at 11 eV due to formation of negative ion (PF_2^-) as reported earlier at 10.3 eV by MacNeil and Thynne [3]. The data sets produced by two formalisms, viz., R matrix and SCOP, are consistent and have identical cross-section value at transition energy (∼7.62 eV). The higher peak value in our total-cross-section data at low energy is attributed to the absence of vibrational channel in our calculation. Including this channel will decrease the cross-section peak as well as broaden the peak thereby bringing the data closer to experimental data of Szmytkowski *et al.* [16]. However the position of the peak value of the cross section is identical in the present case ($M2$) and the measured results of Szmytkowski *et al.* [16] which is around 0.4 eV. Beyond 7 eV, the present data are in good agreement with the data of Szmytkowski *et al.* [16]. Theoretical results of total cross sections of Shi *et al.* [17] are in very good agreement with present data throughout the range of energy reported by them.

In Fig. 6, we present the comparison of total cross section of PF_3 with other structurally similar targets (BF_3, NF_3, NH_3, H_2S, and PH_3) as the comparison for its TCS is very limited. At very low impact energies, generally the elastic cross section observed either shoots high in the case of polar targets or it is very low for nonpolar targets. This feature is clearly seen in Fig. 6. BF_3 is a nonpolar target and hence its elastic cross sections are very low. On the other hand, PF_3 ($\mu = 3.44$ D), NH_3 ($\mu = 1.47$ D), H_2S ($\mu = 0.970$ D), PH_3 ($\mu = 0.580$ D), and NF_3 ($\mu = 0.235$ D) are all polar targets whose cross sections are very high at low energy. While the elastic cross sections for BF_3 and NF_3 are reported by Pastega *et al.* [48] and Joucoski *et al.* [29], respectively, using the Schwinger multichannel method and that of NH_3, H_2S, and PH_3 reported in earlier study by Vinodkumar *et al.* [33] using R-matrix code through Quantemol-N are compared with the PF_3 data in Fig. 6. While the R-T minimum in case of BF_3 is reported at 0.7 eV [48], here in case of PF_3 we have obtained it at 0.33 eV. The other important feature of low-energy cross-

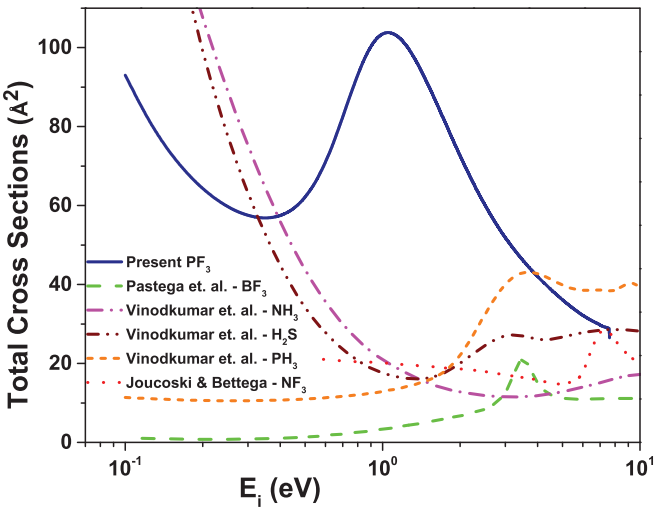

FIG. 6. (Color online) Comparisons of total cross sections of various targets: present PF_3, solid line; NH_3 by Vinodkumar *et al.*, dashed dotted line [33]; H_2S by Vinodkumar *et al.*, dashed dotted dotted line [33]; PH_3 by Vinodkumar *et al.*, short dashed line [33]; NF_3 by Joucoski and Bettega, dotted line [29]; BF_3 by Pastega *et al.*, dashed line [48].

section calculations is the position of the shape resonance which arises due to transient negative ion formation. For BF_3, NF_3, H_2S, PH_3, and PF_3, the positions of shape resonances are found at 3.53, 7.26, 3.07, 3.46, and 1 eV, respectively.

Finally, in Fig. 7 we have compared the total ionization cross section for e-PF_3 scattering obtained using the complex scattering potential ionization contribution (CSP-IC) method developed by our group and using the binary encounter Bethe (BEB) method developed by Kim and Rudd [49]. Since the CSP-IC method is discussed elaborately in previous papers and references therein [33–35], we do not include it here. The basic idea is to extract out the total ionization cross section from the

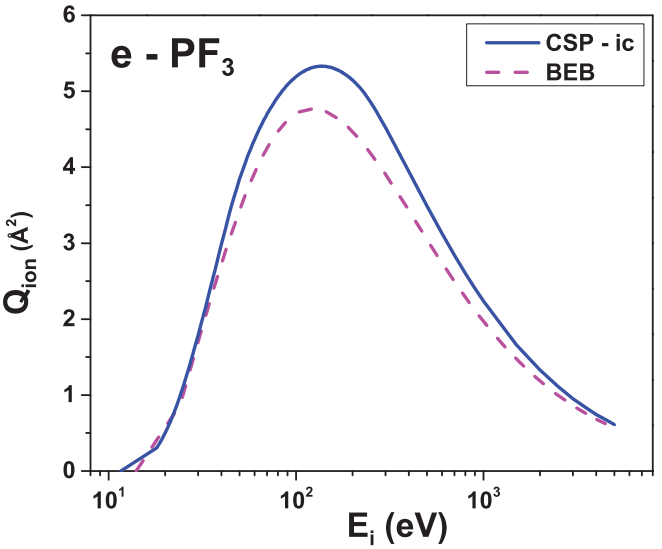

FIG. 7. (Color online) e-PF_3 total ionization cross section: present CSP-IC method, solid line; present BEB method, dashed line.

total inelastic cross section through dynamic ratio [50–52]. The reason for computing the total ionization cross sections using two methods (CSP-IC and BEB) is that there are no other theoretical or experimental data available to compare with the present results. From the curves it is quite clear that data produced by two methods are in good agreement with each other except at the peak. This is attributed to the fact that we have considered IP of PF_3 as 11.70 eV for the CSP-IC method, while for the BEB calculation using Quantemol-N, the IP obtained using Koopman theorem is 14.02 eV. The difference in two IPs can be easily seen at the starting point of both the ionization curves in Fig. 7. The lower the value of IP, the greater the ionization cross section is clearly reflected in Fig. 7. With IP = 11.70 eV (CSP-IC), the peak value of cross section is 5.202 Å^2 at 100 eV and with IP =14.02 eV (BEB), the peak value of the cross section is 4.767 Å^2 at 124 eV.

IV. CONCLUSION

The elastic differential, momentum-transfer, and excitation cross sections are reported for electron impact on PF_3 using the R-matrix method with an adequate target representation. We are able to predict two resonances: $2A''$ having shape resonance at 0.776 eV with width of 0.902 eV and $2A'$ having Feshbach resonance at 13.57 eV of width 1.157 eV. Our calculations are able to predict a Ramsauer-Townsend minimum at 0.33 eV that reflects the accuracy of electron-electron correlation considered in the theoretical treatment. We predicted four vertical excitation states above threshold and the first excitation energy predicted using 6-311G as 6.965 eV and using DZP as 6.971 eV. We employed different target models at low energy. We repeated our calculations with R-matrix radii of 10, 12, and 13 a.u. and observed that the cross-section results increase with increase in R-matrix radii. Also increasing CAS value increases computational time and is used to refine the resonance structure. CAS above 3 does not produce much variation in results.

The energy (7.6 eV) at which the equal values of cross sections provided by the two formalisms (R matrix and SCOP) is considered as the switchover energy. Present results find good agreement with measurements of Szmytkowski *et al.* [16] above 6 eV for all energies reported by them. Below 6 eV, the present results are high due to noninclusion of vibrational channels in our calculation. Present results are also in excellent agreement with theoretical results of Shi *et al.* [17]. In Fig. 7, we have presented total ionization cross sections using the CSP-IC and BEB methods. Results obtained using these two methods are matching well both quantitatively and qualitatively. This work will inspire both theoreticians as well as experimentalists to investigate all the features for e-PF_3 scattering reported in this paper.

ACKNOWLEDGMENTS

The authors are thankful to Professor J. Tennyson for fruitful discussion. M. Vinodkumar and C. Limbachiya acknowledge UGC, New Delhi for Major research project [Project F.No.40-429/2011 (SR)] for financial support under which part of this work is carried out.

[1] I. Schneider, Adv. At. Mol. Opt. Phys. **33**, 183 (1994).
[2] http://www.axcelis.com/sites/default/files/docs/axcelis_safetyconsiderationsimplanter.pdf.
[3] K. A. G. MacNeil and J. C. J. Thynne, J. Phys. Chem. **74**, 2257 (1970).
[4] P. Harland, D. Rankin, and J. Thynne, Int. J. Mass Spectrom. Ion Phys. **13**, 395 (1974).
[5] D. Torgerson and J. Westmore, Can. J. Chem. **53**, 933 (1975).
[6] P. J. Bassett, D. R. Lloyd, I. H. Hillier, and V. R. Saunders, Chem. Phys. Lett. **6**, 253 (1970).
[7] P. J. Bassett and D. R. Lloyd, J. Chem. Soc., Dalton Trans. **(3)**, 248 (1972).
[8] A. W. Potts, H. J. Lempkad, G. Streets, and W. C. Price, Philos. Trans. R. Soc. A **268**, 59 (1970).
[9] J. C. Green, D. I. King, and J. H. D. Eland, J. Chem. Soc. D: Chem. Commun. **17**, 1121 (1970).
[10] J. P. Maier and D. W. Turner, J. Chem. Soc., Faraday Trans. II **68**, 711 (1972).
[11] Y. Zxhao and D. W. Setser, Chem. Phys. Lett. **210**, 362 (1993).
[12] W. C. Price, T. R. Passmore, and D. M. Roessler, Discuss. Faraday Soc. **35**, 201 (1963).
[13] I. H. Hillier and V. R. Saunders, J. Chem. Soc. D: Chem. Commun. 316 (1970).
[14] W. R. Hall and H. F. Hameka, Inorg. Chem. **12**, 1878 (1973).
[15] M. Akbulut, T. E. Madeya L. Parenteau, and L. Sanche, J. Chem. Phys. **105**, 6032 (1996).
[16] C. Szmytkowski, M. Piotrowicz, A. Domaracka, L. Klosowski, E. Ptasinska-Denga, and G. Kasperski, J. Chem. Phys. **121**, 1790 (2004).
[17] D. Shi, J. Sun, Z. Zhu, and Y. Liu, Eur. Phys. J. D **57**, 179 (2010).
[18] J. Tennyson, J. Phys. B: At., Mol. Opt. Phys. **29**, 6185 (1996).
[19] D. Bouchiha, J. D. Gorfinkiel, L. G. Caron, and L. Sanche, J. Phys. B: At., Mol. Opt. Phys. **40**, 1259 (2007).
[20] A. Jain and K. L. Baluja, Phys. Rev. A **45**, 202 (1992).
[21] J. Tennyson, Phys. Rep. **491**, 29 (2010).
[22] Computational Chemistry Comparison and Benchmark DataBase, Release 16a August 2013 NIST Standard Reference Database 101, http://cccbdb.nist.gov/.
[23] *Handbook of Chemistry and Physics*, 76th ed., edited by D. R. Lide (CRC Press, Boca Raton, FL, 1995).
[24] Amine Taleb-Bendiab, Marabeth S. LaBarge, Lawrence L. Lohr, Robert C. Taylor, Kurt W. Hillig, II, Robert L. Kuczkowski and Robert K. Bohn, J. Chem. Phys. **90**, 6949 (1989).
[25] B. Sarpal, K. Pfingst, B. Nestmann, and S. Peyerimhoff, J. Phys. B: At., Mol. Opt. Phys. **29**, 857 (1996).
[26] *Computational Methods for Electron Molecule Collisions*, edited by W. M. Huo and F. A. Gianturco (Plenum, New York, 1995).
[27] B. I. Schneider and T. N. Rescigno, Phys. Rev. A **37**, 3749 (1988).
[28] T. N. Resigno, C. W. McCurdy, A. E. Orel, and B. H. Lengsfield, III, in *Computational Methods for Electron Molecule Collisions*, edited by W. M. Huo and F. Gianturco (Plenum, New York, 1995), p. 144.
[29] E. Joucoski and M. H. F. Bettega, J. Phys. B: At., Mol. Opt. Phys. **35**, 783 (2002).
[30] J. Tennyson and C. J. Nobel, Comput. Phys. Commun. **33**, 421 (1984).
[31] N. Sanna and F. A. Gianturco, Comput. Phys. Commun. **114**, 142 (1998).
[32] F. A. Gianturco and A. Jain, Phys. Rep. **143**, 347 (1986).
[33] C. Limbachiya, M. Vinodkumar, and N. Mason, Phys. Rev. A **83**, 042708 (2011).
[34] H. L. Cox and R. A. Bonham, J. Chem. Phys. **47**, 2599 (1967).
[35] S. Hara, J. Phys. Soc. Jpn. **22**, 710 (1967).
[36] X. Zhang, J. Sun, and Y. Liu, J. Phys. B: At., Mol. Opt. Phys. **25**, 1893 (1992).
[37] R. Lide, *CRC Handbook of Chemistry and Physics* (CRC Press, Boca Raton, FL, 2003).
[38] G. Staszewska, D. W. Schewenke, D. Thirumalai, and D. G. Truhlar, Phys. Rev. A **28**, 2740 (1983).
[39] Minaxi Vinodkumar, Kirti Korot, and P. C. Vinodkumar, Int. J. Mass Spectrom. **305**, 26 (2011).
[40] C. J. Joachain, *Quantum Collision Theory* (North-Holland, Amsterdam, 1983).
[41] Minaxi Vinodkumar and Mayuri Barot, J. Chem. Phys. **137**, 074311 (2012).
[42] Minaxi Vinodkumar, Chetan Limbachiya, Avani Barot, and Nigel Mason, Phy. Rev. A **86**, 012706 (2012).
[43] Minaxi Vinodkumar, Avani Barot, and Bobby Antony, J. Chem. Phys. **136**, 184308 (2012).
[44] L. Andric, I. M. Cadez, R. I. Hall, and M. Zubeck, J. Phys. B: At., Mol. Opt. Phys. **16**, 1837 (1983).
[45] S. I. Chu and A. Dalgarno, Phy. Rev. A **10**, 788 (1974).
[46] N. T. Padial, D. W. Norcross, and L. A. Collins, J. Phys. B: At., Mol. Opt. Phys. **14**, 2901 (1981).
[47] M. A. Morrison, Adv. At. Mol. Phys. **24**, 51156 (1988).
[48] D. Pastega, R. F. da Costa, Marco A. P. Lima, and Marcio, and H. F. Bettega, Eur. Phys. J. D **68**, 20 (2014).
[49] Y. K. Kim and M. E. Rudd, Phy. Rev. A **50**, 3954 (1994).
[50] Chetan Limbachiya, Minaxi Vinodkumar, Mohit Swadia, and Avani Barot, Mol. Phys. **112**, 101 (2014).
[51] Minaxi Vinodkumar, Chetan Limbachiya, Mayuri Barot, Mohit Swadia, Avani Barot, Int. J. Mass Spectrom. **339-340**, 16 (2013).
[52] Minaxi Vinodkumar, Kirti Korot, and Harshad Bhutadia, Int. J. Mass Spectrom. **294**, 54 (2010).